BOLETIN DE LA SOCIEDAD ESPAÑOLA DE
Cerámica y Vidrio
www.elsevier.es/bsecv

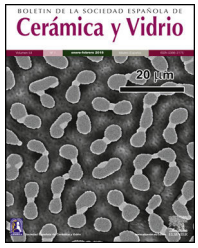

Bioactive scaffolds harnessing ionic modifications to promote osteogenesis and angiogenesis in bone regeneration

Paula M. Riosalido[a], *Marcela Arango-Ospina*[b], *Pablo Velasquez*[a], *Angel Murciano*[c,*], *Aldo R. Boccaccini*[b], *Piedad N. De Aza*[a]

[a] *Institute of Bioengineering, Miguel Hernandez University, Avda. Universidad s/n, 03202 Elche, Spain*
[b] *Institute of Biomaterials, University of Erlangen-Nuremberg, Cauerstr. 6, 91058 Erlangen, Germany*
[c] *Department of Materials, Optical and Electronic Technology, Miguel Hernandez University, Avda. Universidad s/n, 03202 Elche, Spain*

ARTICLE INFO

Article history:
Received 24 March 2025
Accepted 19 May 2025
Available online 7 June 2025

Keywords:
Multilayer scaffolds
Sol–gel
Bone regeneration
Biocompatible

ABSTRACT

This study proposes the modification of multilayer scaffolds based on the SiO_2–CaO–P_2O_5 system by incorporating bioactive ions, such as magnesium or lithium, with the aim of enhancing the cellular processes involved in bone regeneration. Two types of scaffolds, CS04 and CS05, were prepared, varying the amount of MgO (0.38; 0.49% w/w). The prepared scaffolds exhibited an interconnected porous structure, with SiO_2, $Ca_2P_2O_7$ and β-$Ca_3(PO_4)_2$ as predominant crystalline phases, a compressive strength of 1.8 MPa and a porosity above 75%. Bioactivity tests demonstrated that minor variations in the amount of MgO altered the surface topography and bioactive behaviour, resulting in a lamellar microstructure (CS04) and precipitation of hollow HA spheres (CS05). From a biological point of view, the scaffolds proved to be biocompatible, as were their dissolution products at 10 and 100 mg/mL. Both promoted MC3T3-E1 cell proliferation, calcium deposition and osteoblastic differentiation, as reflected by increased ALP activity. In addition, they induced VEGF release in MC3T3-E1, thereby demonstrating their angiogenic potential. Taken together, these results suggest that the scaffolds possess optimal properties for bone regeneration applications.

* *Corresponding author.*
E-mail address: amurciano@umh.es (A. Murciano).
https://doi.org/10.1016/j.bsecv.2025.100447

Andamios bioactivos con modificaciones iónicas para promover la osteogénesis y la angiogénesis en la regeneración ósea

Palabras clave:
Andamios multicapa
Sol-gel
Regeneración ósea
Biocompatible

RESUMEN

Este estudio propone la modificación de andamios multicapa basados en el sistema SiO_2-CaO-P_2O_5 mediante la incorporación de iones bioactivos, como el magnesio o el litio, con e objetivo de potenciar los procesos celulares implicados en la regeneración ósea. Se prepararon dos tipos de andamios, CS04 y CS05, con diferentes concentraciones de MgO (0,38%; 0,49% p/p). Los andamios obtenidos presentaron una estructura porosa interconectada, con fases cristalinas predominantes de SiO_2, $Ca_2P_2O_7$ y β-$Ca_3(PO_4)_2$, una resistencia a la compresión de 1,8 MPa y una porosidad superior al 75%. Los ensayos de bioactividad mostraron que pequeñas variaciones en la cantidad de MgO modificaron la topografía superficial y el comportamiento bioactivo, generando una microestructura laminar (CS04) y a la precipitación de esferas huecas de HA (CS05). Desde una perspectiva biológica, los andamios demostraron ser biocompatibles, al igual que sus productos de disolución a 10 y 100 mg/mL. Ambos andamios estimularon la proliferación celular en MC3T3-E1, la deposición de calcio y la diferenciación osteoblástica, reflejado en un incremento de la actividad de la ALP. Además, se observó liberación de VEGF en MC3T3-E1, sugiriendo su potencial angiogénico. Estos resultados indican que los andamios presentan propiedades óptimas para su aplicación en regeneración ósea.

Introduction

Advancements in medicine and healthcare have significantly increased human life expectancy, leading to a shift in the global demographic profile [1,2]. Consequently, there has been an escalating prevalence of various age-related conditions, including bone fractures, which are frequently attributed to bone fragility and bone loss [2–5]. While individuals with healthy bones generally experience natural healing and regeneration of fractures [6], especially smaller ones, more severe fractures or those complicated by comorbidities such as osteoporosis, diabetes or other chronic inflammatory conditions can overwhelm the bone's ability to regenerate [7,8]. In such cases, external intervention becomes necessary to promote effective healing. This is where the field of biomaterials has made significant advancements, offering promising solutions to enhance bone regeneration [9–11].

The first generation of biomaterials employed for osseous regeneration focused primarily on bioinert materials intended to simply replace lost bone mass [12,13]. Such materials included metallic implants (*e.g.* titanium and stainless steel), synthetic polymers (*e.g.* polymethyl methacrylate and Teflon), and ceramics (*e.g.* alumina and zirconia) [9,12,14]. However, these materials are inert and do not integrate with surrounding tissues, failing to support biological regeneration despite minimising immune responses and foreign body reactions [12,13].

Consequently, the field advanced to second-generation biomaterials, which function not only as structural replacements but are also engineered to elicit controlled responses in the physiological environment, thereby facilitating integration with host bone tissue [12,13]. These materials include synthetic and natural biodegradable polymers, including collagen and polyesters, bioactive bioceramics such as calcium silicate (CS) or bioactive glasses (both silica and non-silica based), as well as bioresorbable bioceramics like tricalcium phosphate (TCP) and hydroxyapatite (HA) [9,12,14,15].

The advent of third-generation biomaterials has led to the development of scaffolds that support bone regeneration while guiding self-healing processes through the induction of favourable cellular responses [9,12,13]. This can be achieved through various strategies, including surface modifications, the use of external stimuli, or the sustained release of soluble factors, such as growth factors, cytokines, or other chemical substances, such us biologically active ions, to enhance tissue repair and regeneration [9].

Despite these advances, there remain significant clinical challenges, particularly in achieving full biological integration and vascularisation of bone grafts, which is imperative for their long-term functionality and success [16,17]. The present study proposes a cost-effective approach to address these issues by means of ionic modification, with the aim of achieving improved biological performance. Through ionic substitutions, it is possible to alter the surface structure, electric charge and reactivity of materials, which may influence its behaviour in physiological environments [18,19]. The bioengineered third-generation scaffolds combine bioactive CS ($CaSiO_3$), resorbable β-TCP ($Ca_3(PO_4)_2$) and the lesser-known vitreous phase P6 ($Ca_2P_6O_{17}$) into a single structure, seeking to create a scaffold that mimics the natural bone structure. Along with the ion-doping strategy, this combination is intended to enhance regeneration related processes of bone tissue and enable implant long-term functionality.

Materials and methods

Materials preparation

The preparation of the multilayer scaffolds was achieved through the implementation of the sol–gel process and the foam replica method, following the methodology illustrated in Fig. 1.

The various stages of this process have been described in detail in previous publications [20,21]. In summary, for the CS core, as well as the CS04 and CS05 outer layers, the raw materials were simply mixed and stirred to facilitate the hydrolysis of the precursors (Fig. 1A). For the P6 and TCP coatings, the mixture was subjected to agitation and heating to facilitate the complete evaporation of the water. Prior to the application of the TCP coating and after the P6 layer, a preconditioning chemical treatment with TRIS (pH 7.35–7.4) was conducted. The TRIS solution was prepared by dissolving 1.17 g of $CaCl_2$ and 7.61 g of tris(hydroxymethyl)aminomethane (tris) in 1 L of distilled water. This step was essential to prevent the excessive reactivity of the glassy phase, which could alter the pH of the solutions during *in vitro* bioactivity and cellular assays [19]. Following the application of each layer, a sintering process was carried out (Fig. 1B). The resulting multilayer scaffolds consisted of four layers: an internal CS ($CaSiO_3$) core, followed by a P6 ($Ca_2P_6O_{17}$) glassy phase coating doped with Li to improve the mechanical strength and tackle the brittleness of the CS core. A third layer of β-TCP ($Ca_3(PO_4)_2$) was then added, followed by an outer CS layer doped with Na, K, and varying amounts of Mg, which defined the nomenclature of the resulting scaffolds. Thus, CS04 contains 0.4 g of $MgCO_3$, while CS05 contains 0.5 g.

Materials characterisation

The X-ray diffraction (XRD) technique was employed for the mineralogical characterisation of the multilayer scaffolds. An automated Bruker-AXR D8 Advance diffractometer, equipped with a secondary graphite monochromator and Cu Kα radiation (1.5418740 Å), was utilised in accordance with the Bragg–Brentano geometry in θ–2θ configuration. The X-ray tube operating conditions were set to 40 kV and 30 mA, and the angle range was set from 15° to 40° with 0.05° increments, with 5 s assigned for each step. Subsequently, the resulting diffractograms were analysed using the Match! software, version 4.1. Peak analysis was conducted using the database provided by the Crystallography Open Database (COD).

The chemical composition was analysed by Fourier Transform Infrared Spectroscopy (FTIR) using a IRAffinity-1S Shimadzu spectrometer. Spectra were scanned in transmittance mode over a wavenumber range of 1400 to 400 cm^{-1} with 40 scans at a resolution of 4 cm^{-1}.

Given the critical role of mechanical resistance and porosity in scaffolds performance, macroporosity was assessed using a water-filled pycnometer. Additionally, a manual compression test was conducted using an SVL-1000N device (IMADA) to evaluate the compressive strength of the scaffolds ($n = 5$).

Additionally, the microstructure of the multilayer scaffolds was examined using a field emission scanning electron microscope (FESEM, ZEISS SIGMA 300 VP) coupled with energy dispersive X-ray spectroscopy (EDS, ZEISS SmartEDX). This was conducted both before and after one week of Simulated Body Fluid (SBF) treatment in accordance with ISO 23317 [22], and based on our previous investigations showing that the resulting bioactive topography promotes cellular proliferation [20,21].

In vitro biocompatibility assessment

Cell culture

Cell assays were conducted on the murine preosteoblast cell line MC3T3-E1. The cells were cultured in 75 cm^2 culture flasks with α-MEM culture medium (Gibco), supplemented with 10% Foetal Bovine Serum (FBS, Corning), 1% penicillin–streptomycin (PS, Gibco) and 1% L-glutamine (L-Glu, Gibco). The flasks were incubated at 37 °C in a humidified atmosphere with 5% CO_2. Once the cells had reached 80% confluence, they were passaged in accordance with standard laboratory practice.

Prior to initiating the cytotoxicity assays, the scaffolds CS04 and CS05 were dry-sterilised in a furnace at 160 °C for a period of two hours. The cytotoxicity was evaluated through two distinct approaches: an indirect approach, in which preosteoblasts were incubated as Culture Medium containing Ionic Dissolution Products (CM-IDP) and a direct approach, whereby cells were seeded on the scaffolds.

Indirect approach

For this purpose, solutions containing powders from powdered scaffolds at a concentration of 10 mg/mL and 100 mg/mL were prepared in supplemented α-MEM, designated as CM-IDP, which was renewed every two days. Following each study interval (1, 3, 7, 14 and 21 days) CM-IDP aliquots were collected and stored at 4 °C for subsequent analysis of the ionic composition by inductively coupled plasma optical emission spectrometry (ICP-OES, Perkin-Elmer Optima 2000^{TM}) and for monitoring of any pH alterations. The remaining medium was entirely removed and replenished with fresh supplemented α-MEM, simulating the clearance processes observed *in vivo*. This approach enabled the extraction of the dissolution products after each interval, preventing its accumulation and facilitating an understanding of its potential *in vivo* effects.

In parallel and 24 h prior to assay commencing, preosteoblasts were seeded at a density of 5000 cells/cm^2 to allow cell attachment with supplemented α-MEM. Subsequently, the supplemented α-MEM was removed from the wells and replaced with the CM-IDP, except for the control wells, where it was renewed. The aliquots for ICP-OES and pH measurement were also collected. After 24 h of exposure (day 1), the viability assay WST-8 (CCK-8, Sigma–Aldrich) was performed and absorbance was read (FLUOstar Omega, BMG LabTech).

Afterwards wells were rinsed with Dulbecco's Phosphate Buffered Saline (DPBS, Gibco) and incubated with CM-IDP except from control wells. This procedure was repeated on days 3, 7, 14 and 21 of the study.

To complement WST-8 assay, cells were live stained with calcein acetoxymethyl-ester (Calcein AM, Invitrogen), fixed

A

MATERIALS	CS Core	P6	TCP	CS04	CS05
PRECURSORS					
• TEOS (mL)	19.28	-	-	19.28	19.28
• TEP (mL)	-	18.46	10.96	-	-
• $CaCO_3$ (g)	8.62	3.72	8.64	8.62	8.62
SOLVENTS (mL)					
• Ethanol	5	5	5	5	5
• H_2O	20	20	20	20	20
CATALYZER (mL)					
• HCl 37%	1	2	2	1	1
DOPANTS (g)					
• Li_2CO_3	-	1	-	-	-
• $MgCO_3$	-	-	-	0.4	0.5
• Na_2CO_3	-	-	-	0.5	0.5
• K_2CO_3	-	-	-	0.5	0.5

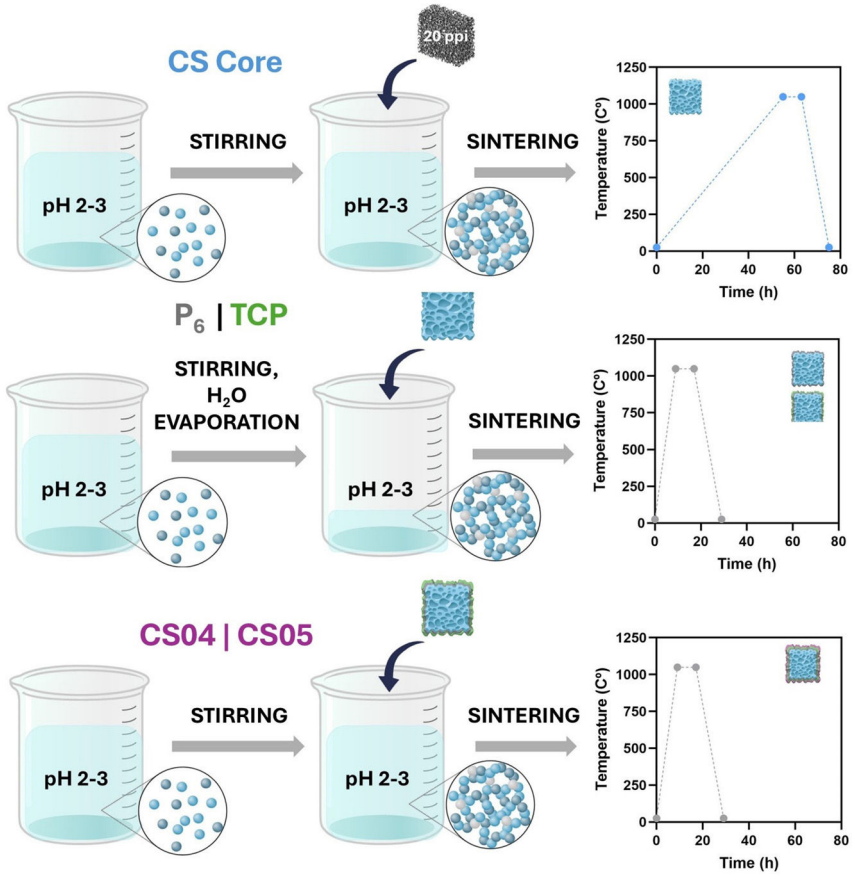

B

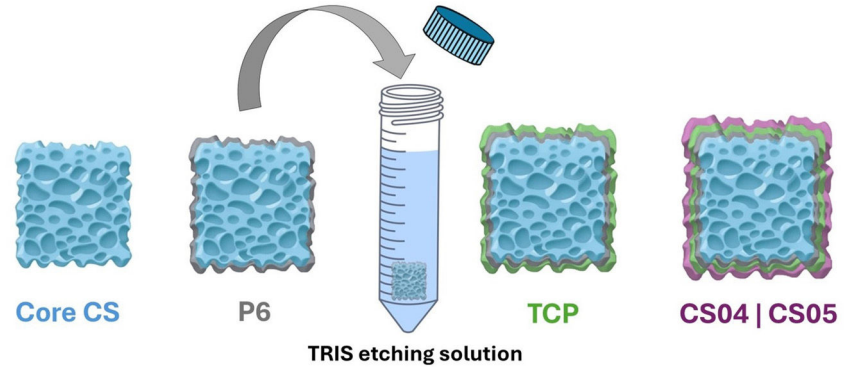

Fig. 1 – Diagram of the multilayer scaffold preparation process: sol–gel method and sintering (A); assembly of layers and scaffold preconditioning (B).

with 3.7% formaldehyde for and finally stained with DAPI (Sigma Aldrich) to evaluate their morphology after DP-CM exposure. Images were adquired through a Axio Scope A.1, Carl Zeiss Fluorescence Microscope.

Direct approach

MC3T3-E1 cells were plated at a density of 5000 cells/cm^2 onto the scaffolds CS04 and CS05. WST-8 assays were conducted at 1, 3, 7, 14, and 21 days, as previously described.

After the various study periods, the cells were subjected to a process of fixation and subsequent examination using SEM, with the objective of assessing the morphology of the cells. Two distinct fixation solutions were utilised for 1 h each: the initial solution consisted of 0.1% glutaraldehyde, 2% formaldehyde and 5% sucrose, while the second solution included 0.3% glutaraldehyde, 3% formaldehyde. Subsequently, a dehydration process was conducted utilising a series of ethanol solutions, ranging from 30% to 99.9%, with each concentration applied for a period of 30 min. Subsequently, the samples were subjected to critical point drying (Leica EM CPD300) and analysed using SEM (Auriga CrossBeam, Carl Zeiss).

Osteogenic assessment

For osteogenic assays, 50 μg/mL L-ascorbic acid (Sigma Aldrich), 10 mM β-glycerophosphate (Sigma), and 10 nM dexamethasone (Sigma Aldrich) were added to the supplemented α-MEM to create an osteogenic differentiation medium for culturing MC3T3-E1.

Alizarin red staining (ARS) was employed to assess the deposition of calcium on CS04 and CS05 scaffolds. In brief, cells were seeded on scaffolds for 7, 14, and 21 days, after which they were fixed with 3.7% formaldehyde for 1 h, stained for 10 min with ARS (2%; pH 4.3) in darkness, and rinsed with DPBS and dH$_2$O as many times as necessary until the washing solution was transparent. A qualitative analysis was conducted using images of the scaffolds obtained through an optical microscope (Primo vert, Carl Zeiss). For the quantitative analysis, a 10% acetic acid solution was employed for 30 min with gently shaking to remove the stain, and the absorbance was subsequently quantified at 405 nm. In consideration of the elevated calcium content of the scaffolds, the baseline staining of the scaffolds was assessed and employed for the standardisation of the values.

To assess the impact of multilayer scaffolds on osteoblast differentiation, the specific alkaline phosphatase (ALP) activity was quantified at 3, 7, 14 and 21 days. The activity of ALP was evaluated through an enzymatic and colorimetric assay, whereby the formation of yellow p-nitrophenol (pNP) resulting from the hydrolysis of nitrophenylphosphate (p-NPP) by ALP was quantified. In this regard, the cells were lysed and subjected to centrifugation to obtain the proteins present in the supernatant. Subsequently, 150 μL of the supernatant were combined with 50 μL of the ALP mixture (1 M Tris, 2 mM $MgCl_2$, 9 mM p-NPP), which provides the requisite conditions and substrate for ALP. The mixture was incubated at 37 °C until a colour change was observed, after which 1 M NaOH was added to terminate the reaction. The absorbance was determined at a wavelength of 405 nm. Concurrently, the total protein content of the supernatants was determined through the Bradford assay. For this purpose, 25 μL of cell lysates supernatants were mixed with 975 μL of the Bradford reagent, which were incubated for 10 min in the dark. The absorbance was measured at 595 nm. The specific ALP activity was calculated based on the ALP measurement and the Bradford assay and is presented as the activity of hydrolysing a certain amount of nanomolar pNPP per minute and milligramme of total protein.

Angiogenic assessment

In order to investigate the potential angiogenic impact of multilayer scaffolds on the MC3T3-E1 cell line, the RayBio® Mouse VEGF-A ELISA Kit was utilised to quantify the liberation of VEGF in cell supernatants, in accordance with the instructions provided by the suppliers [23]. The data are presented as the percentage of VEGF secretion relative to the control mean (considered as 100%) for each time point of the study.

Statistical analysis

One-way ANOVA was utilised to compare groups at each time point. Following this, *post hoc* analyses were carried out using Tukey's test to determine specific differences between the groups. Statistical significance was established with an alpha level of 0.05 and a 95% confidence interval. Results are expressed as mean ± standard deviation (SD). All statistical analyses were performed using GraphPad version 10.3.1.

Results

The resulting scaffolds exhibited an interconnected porous structure with final dimensions of 0.9 ± 0.1 cm in diameter and 0.8 ± 0.1 cm in height (inset Fig. 2A).

Materials characterisation

The XRD patterns (Fig. 2) revealed the crystalline composition of the multiphasic scaffolds which included calcium phosphates, silicates, and magnesium-rich phases. Among the calcium phosphates, characteristic peaks of calcium pyrophosphate ($Ca_2P_2O_7$) (COD 96-100-1557) were observed at $2\theta = 29.6°$, 33.5°, while those of β-tricalcium phosphate (β-TCP, $Ca_3(PO_4)_2$) (COD 96-151-7239) appeared at $2\theta = 31.01°$ and 34.3°. For the silicates, wollastonite ($CaSiO_3$) (COD 96-900-5779) was identified with peaks at $2\theta = 29.9°$, while cristobalite (SiO_2) (COD 96-900-8225) was detected at $2\theta = 21.9°$.

The magnesium-rich phases included akermanite (AK, $Ca_2MgSi_2O_7$) (COD 96-900-6942), with peaks at $2\theta = 31.1°$ and whitlockite (WH, $Ca10.115Mg0.385(PO_4)_7$) (COD 96-901-2137) displays characteristic diffraction signals that are slightly shifted to the right with respect to those of β-TCP, at $2\theta = 31.1°$ and 27.8°. The magnesium substitution within whitlockite results in lattice parameter distortion, leading to slight shifts in its diffraction peaks in comparison to the stoichiometric β-TCP. The superposition of the peaks from whitlockite and β-TCP results in a broadening effect in the XRD patterns, as observed at $2\theta = 31°$ and 27.8° (*e.g.*).

Fig. 2B depicts the FTIR spectra of scaffolds CS04 and CS05. The presence of Si—O—Si and PO_4^{3-} groups was confirmed,

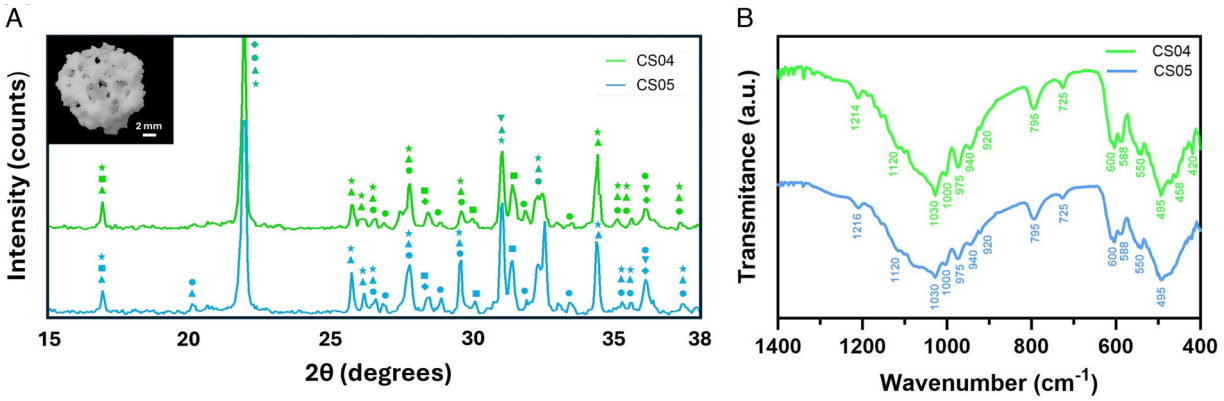

Fig. 2 – Materials characterisation. Chemical composition assessed using XRD (a) and FTIR (b). A small inset showing an optical image of the scaffold (top view) is included in (a). XRD legend: ♦ SiO_2; ● $Ca_2P_2O_7$; ▲ $Ca_3(PO_4)_2$; ■ $CaSiO_3$; ★ $Ca_{10.115}Mg_{3.85}(PO_4)_7$; ▼ $Ca_2MgSi_2O_7$.

with some overlapping bands. Furthermore, the presence of $P_2O_7^{2-}$ and HPO_4^{2-} groups was identified.

The PO_4^{3-} groups gave rise to the appearance of several bands, which were associated with various vibrational modes: (i) asymmetric stretching peaks at 1000 and 1030 cm^{-1}; (ii) symmetric stretching at 940 and 975 cm^{-1}; and (iii) bending modes at 600, 588 and 550 cm^{-1}. Furthermore, the HPO_4^{2-} group was identified at 920 cm^{-1}.

With regard to the Si—O—Si group, bands were observed in two principal regions. (i) asymmetric stretching or bending in the range 1216–1000 cm^{-1}, and (ii) symmetric stretching, with bands at 975 and 795 cm^{-1}. In addition to these regions, a Si—O—Si rocking band was also observed at 458 cm^{-1}, as well as a new band corresponding to Si—O—NBO at 920 cm^{-1}.

Finally, the pyrophosphate group ($P_2O_7^{2-}$) was present, with signals at 725, 920 and 1216 cm^{-1} detected in both scaffolds.

A comparison of the two spectra reveals that, despite the similarity in background and the majority of peaks, the bands corresponding to the phosphates in CS05 are markedly broader than those observed in CS04.

With regard to their physical properties, CS04 and CS05 exhibited comparable characteristics. Both exhibited a compressive strength of 1.8 ± 0.1 MPa and a porosity greater than 75%. CS04 demonstrated a macroporosity of 76 ± 2%, while CS05 revealed a slightly higher macroporosity of 77 ± 1%.

The SEM characterisation of the microstructure of the scaffolds prior and after SBF exposure is shown in Fig. 3. The surface of CS04 exhibits elongated and interconnected channels, which manifest a lamellar appearance. The lamellae were composed of Ca–P–Si grains, with a similar contribution of P and Si resulting in a Ca/P+Si of 0.7 ± 0.1. In terms of dimensions, the lamellas range from 5 to 10 μm in length and 1 to 3 μm in thickness, exhibiting an overall rough texture and irregular edges.

In contrast, CS05 displayed a surface characterised by a granular texture and elongated grains, with a rod shape morphology ( ), rich in calcium and silicon (Ca/Si ratio of 2 ± 0.1) (Fig. 3). These rod-shaped Ca–Si structures were observed to have a length of between 5 and 15 μm and a width of between

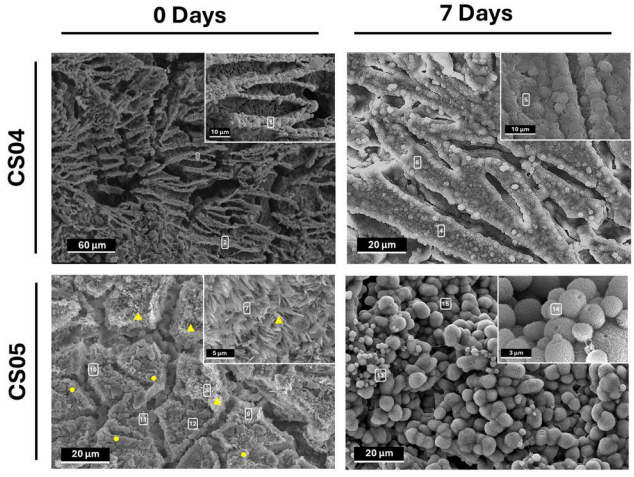

Fig. 3 – Surface analysis. FESEM-EDS micrographs depicting the microstructure of the scaffolds prior to (0D) and following 7 days of SBF exposure.

1 and 2 μm. Big angular Ca–P–Si grains ( ) were also detected with a Ca/P+Si ratio of 0.6 ± 0.1.

Following a seven-day immersion period in SBF, both scaffolds exhibited evidence of mineral deposition on their surfaces. In the case of CS04, the original lamellar structure is still discernible, but it is now covered by a precipitate. The elemental composition of the mineral layer, as determined by EDS, indicates a composition based on Ca and P (Ca/P of 1.6 ± 0.1), with variable amounts of substituent ions such as Mg^{2+} (0.8 ± 0.1 at%), SiO_4^{4-} (2.6 ± 0.2 at%) or Na^+ (1.2 ± 0.1 at%) which are typically found in biological apatites [24,25]. However, CS05 displays a distinctive bioactive behaviour. The surface is observed to be densely covered with spherical Ca–P particles (Ca/P ratio of 1.7 ± 0.1), with a diameter of approximately 1–3 μm. A close-up view of the precipitated particles reveals the presence of a central cavity, suggesting the presence of a hollow structure. Furthermore, the precipitates were found to contain Mg^{2+} (0.9 ± 0.1 at%), SiO_4^{4-} (2.7 ± 0.1 at%) and Na^+ (1.2 ± 0.1 at%) dopants upon elemental examination

Table 1 – EDS analysis of the scaffold surface before and after 7 days of immersion in SBF.

EDS spot	Atomic %				
	Ca	P	Si	Mg	Na
1	38.6	34.3	27.1	–	–
2	43.6	30.4	26	–	–
3	41.3	25.2	33.5	–	–
4	60.2	35.1	2.8	0.7	1.2
5	57.3	38.2	2.5	0.9	1.1
6	58.1	36.9	2.7	0.9	1.4
7	67.7	–	32.3	–	–
8	65.5	–	34.5	–	–
9	66.2	–	33.8	–	–
10	37.5	20.8	41.7	–	–
11	40.7	21.2	38.1	–	–
12	39.3	21.5	39.2	–	–
13	61	34.2	2.6	0.9	1.3
14	58.2	37.2	2.8	0.8	1
15	59.3	36	2.6	1	1.2

(Fig. 3B). Lithium and potassium were found to be below the equipment's detection limit. For further details regarding the EDS analysis, see Table 1.

In vitro biocompatibility assessment

Following the physicochemical characterisation of the scaffolds, cell viability and cell morphology was evaluated to assess scaffolds biocompatibility.

Firstly, an indirect method was employed to evaluate the cytocompatibility of CM-IDPs *in vitro* and their effect on cell behaviour. This approach was used to assess the effect of the scaffolds on neighbouring cells, which also contribute to the deposition of new ECM. In order to achieve this, the solutions described in Section "Indirect approach" were prepared and the ionic variations of the CM-IDPs were monitored over 21 days (Fig. 4).

The ion release patterns observed in the scaffolds can be categorised into three distinct behaviours: release, absorption, and stability. For releasing ions, calcium was leaked in greater amounts at higher concentrations (100 mg/mL) compared to lower concentrations (10 mg/mL), with CS04 showing a higher release at the same concentration. A comparable trend was observed for silicon, which was released to a greater extent at higher concentrations, with CS04 exhibiting a higher release than CS05. A direct relationship between lithium liberation and concentration was also observed, albeit with CS05 releasing more lithium. It was observed that the released ions remained within a range of 30 mg/mL above the basal level.

With regard to the absorbed ions, magnesium demonstrated enhanced incorporation into the sample at elevated concentrations, with a slight increase in uptake observed for CS05. Conversely, phosphorus exhibited higher levels of precipitation or uptake at higher concentrations, particularly for CS04. It is noteworthy that phosphorus and silicon demonstrated an inverse relationship; as one increased, the other decreased.

Finally, sodium and potassium concentrations fluctuated but remained close to baseline levels throughout the study. As anticipated, the ionic variations resulted in alterations in the mean pH. With regard to CS0X at 100 mg/mL, there is a tendency towards alkalinisation in comparison to the control (pH 8.3). However, for CS0X at 10 mg/mL, the pH variations are not particularly marked and remain closer to the baseline. While CS04 initially basifies the pH of the medium, CS05 acidifies it. At day 21, both pH values are almost equal, indicating a slight acidification.

The results of the WST-8 assay show that CS04 and CS05 scaffolds, through an indirect approach and direct approach, are biocompatible and favour cell viability of murine MC3T3-E1 preosteoblasts (Fig. 5).

Fig. 5A illustrates a gradual increase in cell population over time in each treatment group, indicating that the scaffold dissolution products are cytocompatible. A more detailed analysis reveals that, during the initial three-day period, cell viability is slightly lower in the treatment groups relative to the control, particularly for CS04 at 100 mg/mL. However, these differences are not statistically significant. By day 7, cell viability is notably higher in all treated groups, with CS05 at both concentrations demonstrating statistically higher and significant values in comparison to the control and CS04 at the same concentration. From day 14 onwards, cell proliferation appears to reach a saturation state, given that the 2D culture has occupied the available surface area, thereby limiting further growth. However, in the case of CS04 100 mg/mL, due to the smaller initial cell population, a slight increase in viability was still observed, likely because there was still some surface area available for proliferation.

In the direct approach (Fig. 5B), increasing cell viability is observed over time for all scaffolds tested, confirming their cytocompatibility. Although no statistically significant differences were found between CS04 and CS05, a slightly higher cell viability was generally observed for CS05.

Fig. 6A depicts the behaviour of MC3T3-E1 preosteoblasts treated with the different CM-IDP preparations over a seven-day period. The assay was limited to day 7 because, as indicated in Fig. 5A, a saturation point was reached due to complete colonisation of the culture plate, which prevented the visualisation of individual cell morphology and provided no additional information. At the 24-h mark, cell adhesion is evident across all treatment groups. The cells exhibit their characteristic spindle-like morphology, indicating good

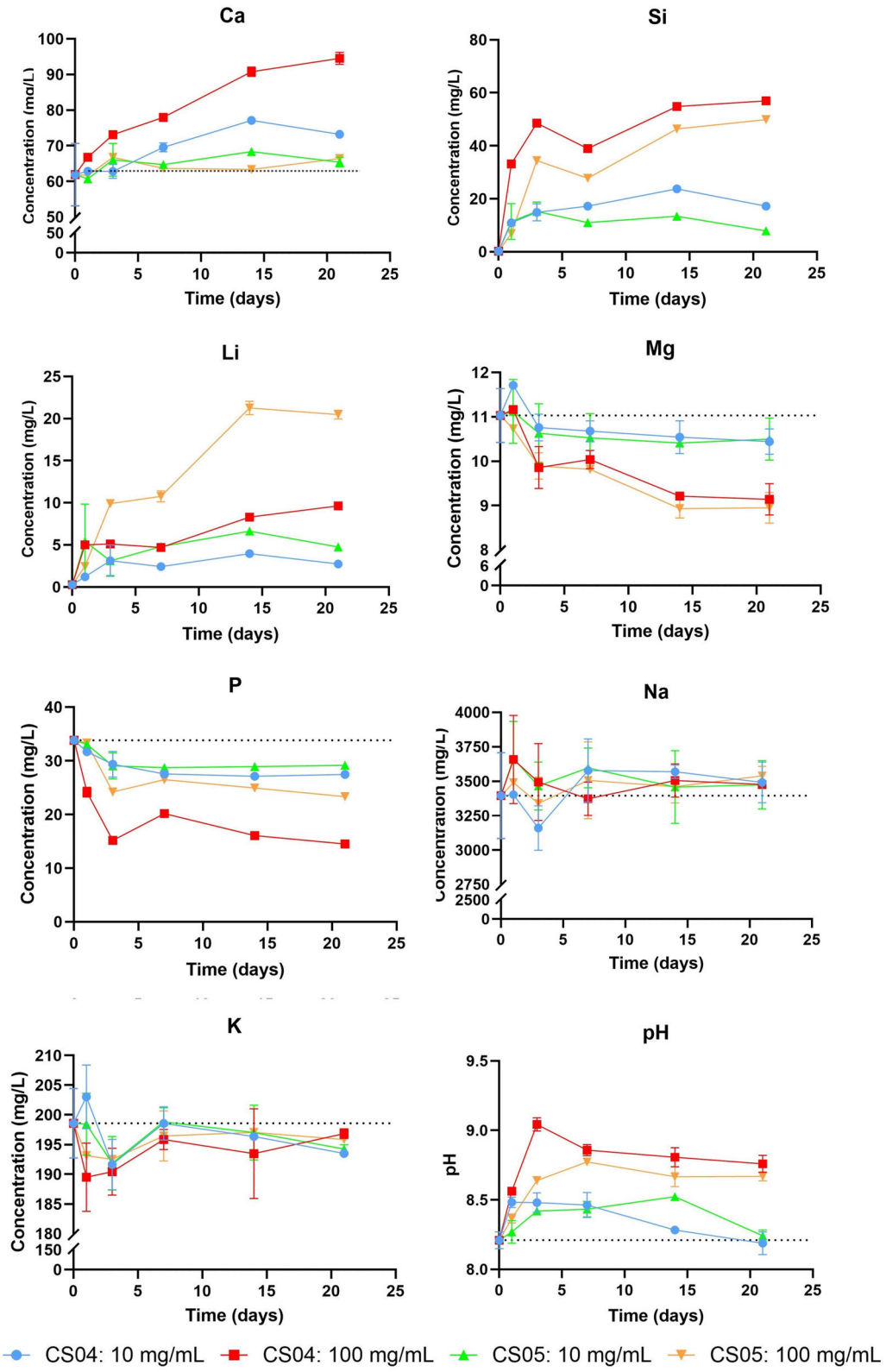

Fig. 4 – Monitoring of ionic concentration and pH variations of CM-IDP over 21 days.

cellular health. However, a lower cell density is observed for CS04-100 mg/mL compared to the control and other treatments, a trend that persists throughout the seven-day study period. Additionally, a consistent increase in cell population is noted over time, with the cells progressively spreading and nearly reaching confluence by day seven.

As shown in Figure 6B, the SEM micrographs demonstrate evidence of cell adhesion within 24 hours. While the

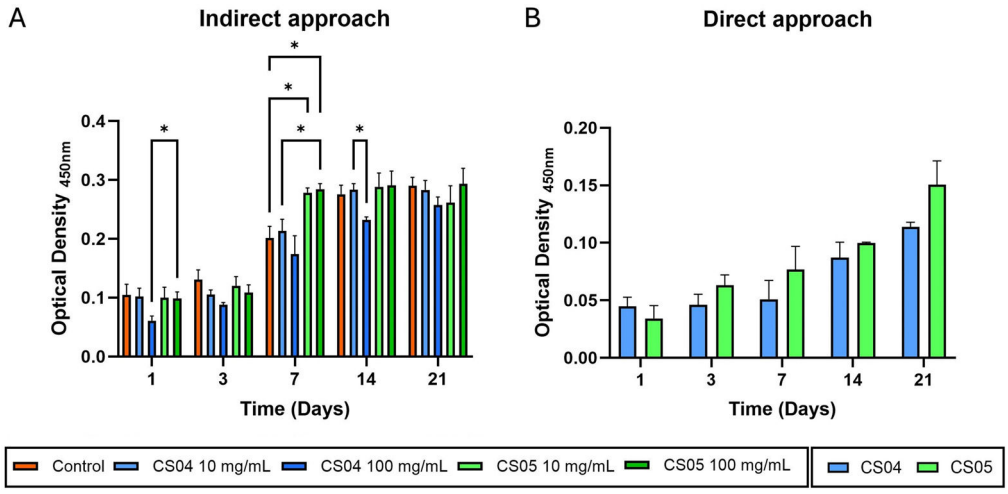

Fig. 5 – Results of the cell viability assay WST-8 from an indirect (A) and direct approach (B).

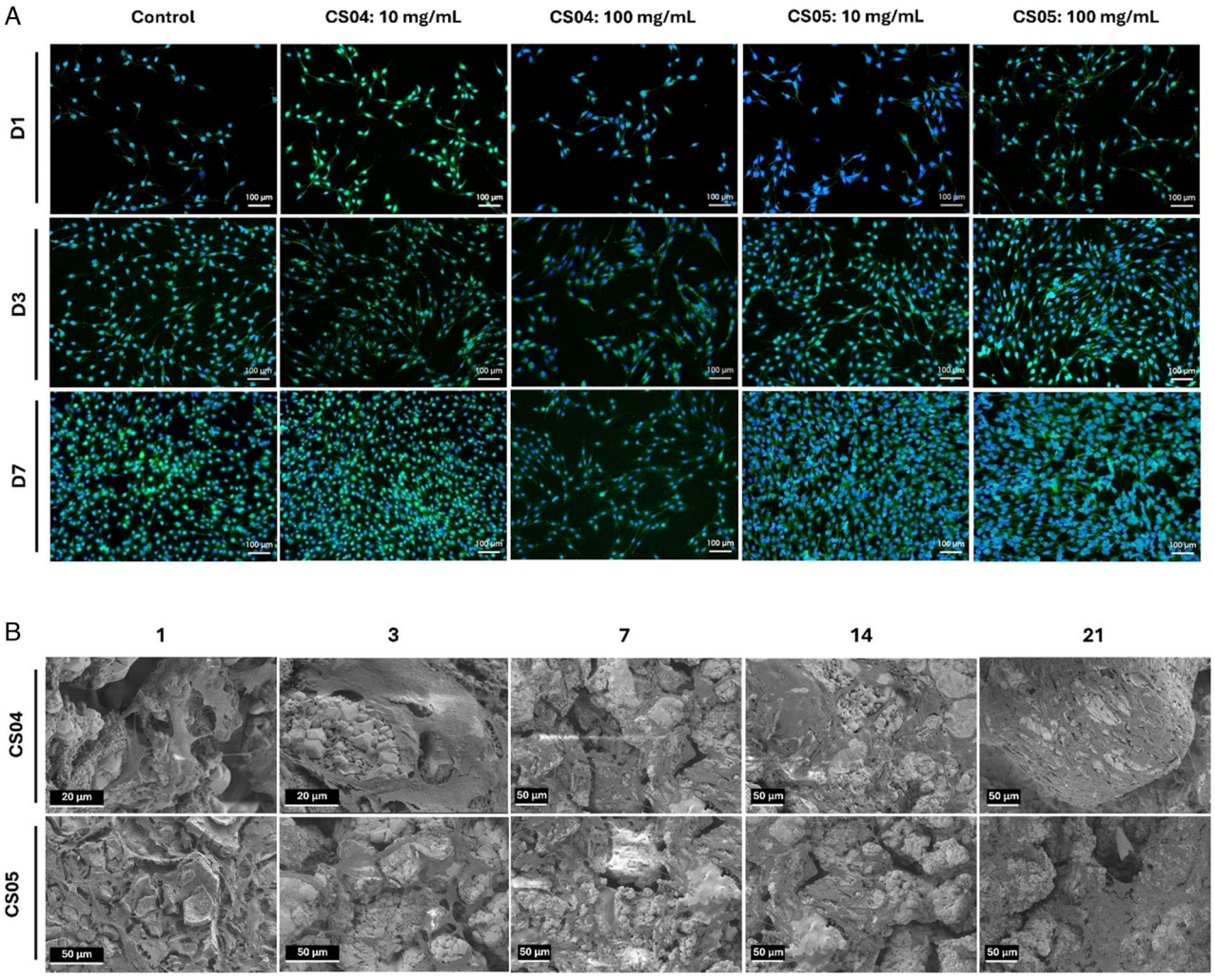

Fig. 6 – Evaluation of MC3T3-E1 morphology upon exposure to CM-IDP (A) and plated on scaffolds CS04 and CS05 (B).

morphology varies, displaying both star-shaped cells and spindle-like cells (e.g., CS0X, 1D), which are particularly evident in CS05 at 21 days, the cells in all cases appear flattened and well-spread on the scaffold surface. Furthermore, well-defined filopodia are evident, indicating a robust interaction with the material. With time, the cells are seen to disperse throughout the surface of the scaffold, although they do not achieve complete confluence.

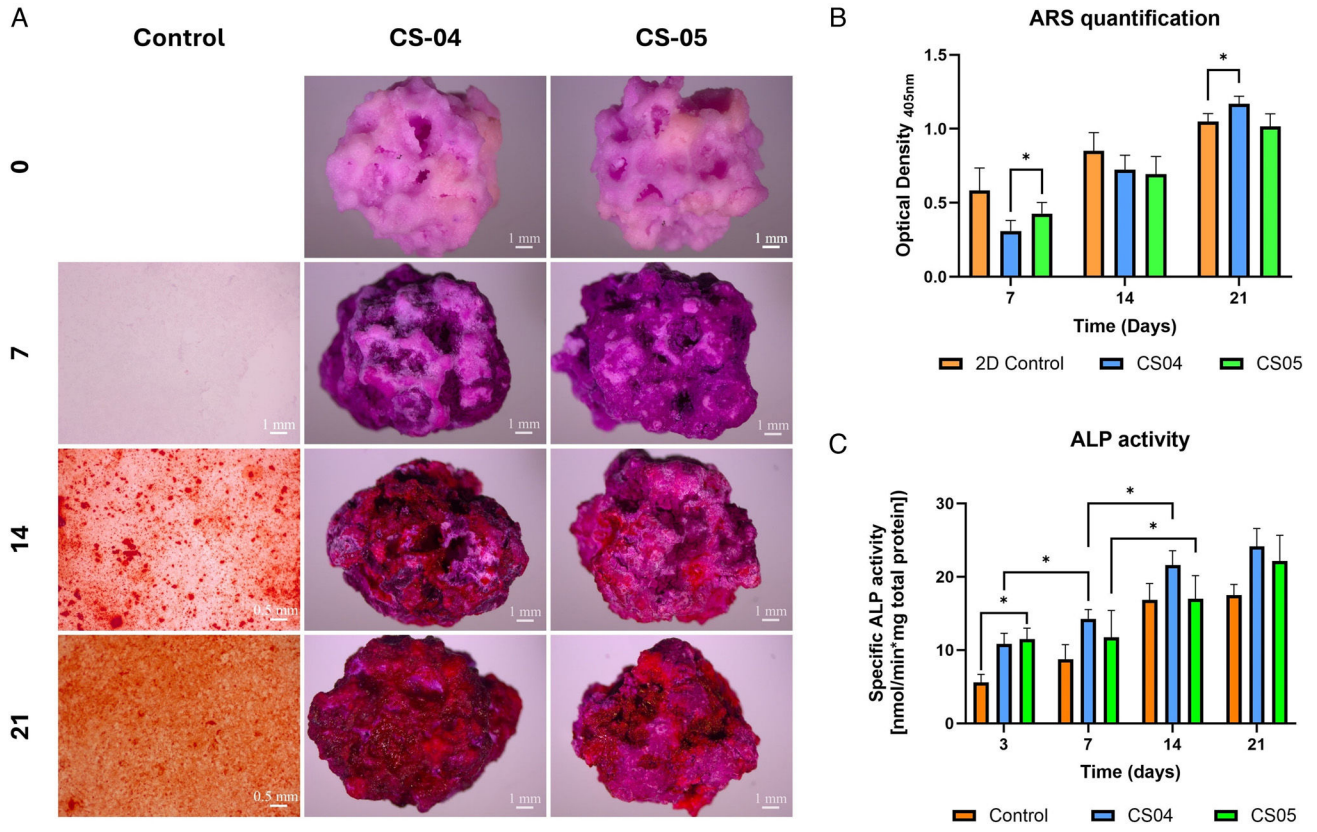

Fig. 7 – Osteogenic assessment. Qualitative (A) and quantitative (B) ARS staining results, along with the quantification of ALP specific activity (C).

Osteogenic assessment

To assess the osteogenic potential of the scaffolds, ARS and specific quantification of ALP activity were performed (Fig. 7). To initiate the study, ARS staining was performed on the cell-free scaffolds to avoid background interference during the mineralisation assessment. The staining at day 0 generated a basal pinkish hue which subsequently evolved into a more intense purple on day 7. Finally, the scaffolds exhibited a reddish hue by day 14, with an intensification observed after 21 days, particularly at CS04. Fig. 7B quantifies the ARS staining, demonstrating a notable elevation in optical density (OD_{405}) for the scaffolds on day 14.

With regard to ALP activity, an overall enhancement in specific activity was observed in cells seeded on the scaffolds in comparison to the 2D control, indicating an augmented osteoblastic activity in cells exposed to the scaffold.

Angiogenic assessment

The angiogenic potential of the CS04 and CS05 scaffolds was evaluated by quantifying the release of VEGF in cell supernatants, with the release observed in the control group considered as the 100% reference (Fig. 8). It was observed that, while no statistically significant differences were found between the control cells and those seeded on the scaffolds during the first week of the study, after 14 days, these differences became pronounced, with VEGF release levels of 160% for CS05 and 170% for CS04. These differences remained significant at 21 days, with an increase in the level of significance.

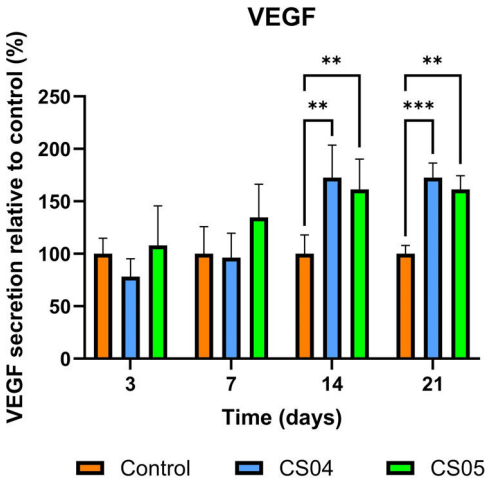

Fig. 8 – Assessment of angiogenic potential. VEGF secretion in the supernatants of cells cultured on 2D control or scaffolds CS04 and CS05.

Discussion

In this study, the design of third-generation multilayer porous scaffolds aims to optimise scaffold performance by combining

phases that closely mimic the mineral composition and physiological properties of bone tissue. The strategic incorporation of inorganic elements such as magnesium, lithium and other bioactive ions into the scaffold matrix has the potential to significantly enhance the bioactivity of the materials, the biochemical cell-material interactions, as well as the mechanical strength and biological performance of the materials.

The resulting scaffolds with a final diameter of 0.9 ± 0.1 cm and a height of 0.8 ± 0.1 cm displayed an interconnected porous structure. According to the experimental XRD spectra, the predominant phases identified in the scaffolds were $Ca_2P_2O_7$, β-$Ca_3(PO_4)_2$, SiO_2, together with $CaSiO_3$, $Ca_{10.115}Mg_{0.385}(PO_4)_6$, and $Ca_2MgSi_2O_7$ to a lesser extent (Fig. 2A). While CS and β-TCP were initially formulated, the additional phases were formed as a result of ionic doping with magnesium (*e.g.*, $Ca_{10.115}Mg_{0.385}(PO_4)_6$ and $Ca_2MgSi_2O_7$) or due to ionic migration between layers during the sintering process (*e.g.*, $Ca_2P_2O_7$ and SiO_2). The latter process can be described as a calcium migration phenomenon induced by the interaction between CS and the amorphous phosphate coating P6. At 1050 °C, calcium migration from $CaSiO_3$ to $Ca_2P_6O_{17}$ destabilises CS, resulting in its transformation to SiO_2. At the same time, the ultraphosphate phase $Ca_2P_6O_{17}$, which exhibits structural disorder, is transformed into a more stable crystalline phase, calcium pyrophosphate ($Ca_2P_2O_7$), by incorporating calcium from the CS [26].

In consideration of the *in vivo* behaviour of each material, the scaffolds incorporate rapidly resorbable phases, including β-TCP and WH [12,14]. These phases facilitate the release of essential ions that promote matrix mineralisation and other osseous-related processes [13,27,28]. They also contain bioactive materials, such us CS and AK, which enhance the scaffold's capacity to bond with hard tissue [28,29]. Additionally, the incorporation of calcium pyrophosphate and silica plays a pivotal role in improving the mechanical properties and modulating the degradation rates of the scaffold, respectively, thus ensuring compatibility with physiological processes [27,29,30].

The presence of these phases was additionally corroborated by FTIR (Fig. 2B). The signals at 724 cm^{-1}, 919 cm^{-1} and 1208 cm^{-1} indicate the presence of the pyrophosphate group, which is characteristic of $Ca_2P_2O_7$. Additionally, another phosphate vibrational mode, PO_4^{3-}, was identified, which is associated with the β-TCP and WH phases. The Si—O—Si group was also detected, which is indicative of the cristobalite, calcium silicate and akermanite phases.

As mentioned above, the crystal structures of β-TCP and WH are closely related, resulting in almost identical XRD patterns. Therefore, reliable identification of WH is not possible without the use of vibrational spectroscopy, which allows the observation of signals from the $HPO4^{2-}$ group at 920 cm^{-1} (Fig. 2B). This structural unit can be used as a reliable spectral marker as it is only present in the crystal structure of WH [31].

FTIR spectra also revealed that increasing the magnesium content broadened the phosphate bands and reduced their intensities, reflecting reduced crystallinity due to competition between Mg^{2+} and Ca^{2+} for binding with pyrophosphate ($P_2O_7^{2-}$) and phosphate (PO_4^{3-}) [32]. The ionic radius mismatch between Mg^{2+} and Ca^{2+} caused lattice distortions leading to a disruption of crystallinity.

With regard to the physical characterisation of the scaffolds, a compressive strength of 1.8 ± 0.1 was observed, along with a porosity over 75%, which is in accordance with the requirements for bone tissue regeneration applications [16,33]. While the compressive strength is lower than that of cortical bone, it is comparable to that of trabecular bone (1.7–7.5 MPa) [34]. In particular, the mechanical strength is expected to increase as new mineral phase is deposited, compensating for scaffold degradation, as reported in previous studies of ceramic scaffolds *in vivo* [35].

The porosity of the scaffolds is beneficial for facilitating angiogenesis and vascular infiltration, which are essential for the transportation of nutrients, oxygen and growth factors [10,16,33]. In addition, increased porosity increases the surface area of the scaffold, promoting enhanced cell infiltration, adhesion and migration – key processes for effective bone regeneration [17,36].

However, porosity should be coupled with an appropriate microstructure that facilitates optimal cell-material adhesion while promoting the deposition of bone-like minerals. Both scaffolds, CS04 and CS05, exhibited surface characteristics consistent with materials tailored for bone regeneration (Fig. 3) [9,13,16,17]. The lamellar structure of CS04, composed of calcium silico-phosphate crystals, provides nucleation sites for HA formation due to its silicon content. Although these lamellae are not strictly classified as "pores", they create voids that significantly increase the surface area of the scaffold. Similarly, CS05 had a Ca–Si based surface which also provided nucleation sites for mineral deposition.

Subtle variations in Mg content were found to influence both the scaffold topography and the bioactive behaviour. After one week in SBF, both scaffolds showed deposition of apatite-like precipitates enriched in Mg^{2+}, SiO_4^{4-} or Na^+ as substitutes for Ca^{2+}, PO_4^{3-} and OH^- ions and deviating from the stoichiometric formula of hydroxyapatite, $Ca_{10}(PO_4)_6(OH)_2$. For CS04, the lamellar structure was maintained under these precipitates, whereas CS05 developed hollow microspheres (1–3 μm) on its surface. Similarly, Bauer et al. reported that the incorporation of Mg^{2+} ions into calcium phosphate scaffolds resulted in surface morphology modifications and precipitation of microspheres during SBF tests, with sizes tunable as a function of Mg content [32].

The chemical composition of these apatite-like precipitates underlines the ability of the scaffold to mimic physiological bone mineralisation, considering that biological apatites are deficient in calcium [24,25]. This ability is essential to allow the scaffold to integrate with the surrounding bone. In addition, these biomimetic, non-stoichiometric apatites offer distinct advantages over stoichiometric synthetic HA. While synthetic HA is widely used for implants due to its high stability, its low solubility results in slower resorption rates compared to physiological tissue regeneration [37]. In contrast, biomimetic substituted HA ensures higher biodegradability and bioactivity, as well as sustained release of biologically active ions [38].

The field of ion-releasing scaffolds for biomedical applications has experienced significant growth over the past two

decades, driven by the recognition of the potential benefits of ion release for tissue repair therapies [28].

In this regard, the concentration of constituting ions (P, Si and Ca^{2+}) as well as doping ions (Li^{+}, Mg^{2+}, Na^{+} and K^{+}) were monitored over a 21-day period in a non-cumulative degradation study (Section "Indirect approach"). The ions that were predominantly released were calcium, silicon and lithium (Fig. 4).

Calcium plays an essential role in bone and its metabolism, as a key component of the mineral phase in the form of HA [33]. Previous research has shown that the release of calcium *in vitro* is associated with enhanced osteogenic differentiation [39,40], proliferation of bone marrow stem cells [40], and increased ALP activity [28,41], among other beneficial effects.

Silicon has been extensively documented to play a pivotal role in a number of biological processes, including bone mineralisation, collagen synthesis and osteogenesis [12,29,42,43]. These processes include ALP expression and the early differentiation of osteoblasts, as previously reported by Sun et al. [44]. Additionally, Si ions have been demonstrated to facilitate the formation of apatite layers, thereby enhancing bioactivity [12,29].

Although lithium is a toxic alkaline metal, it has been demonstrated to exhibit angiogenic and osteogenic properties when incorporated into bioactive glasses in both *in vitro* and *in vivo* conditions [45–47]. Tal et al. demonstrated that lithium concentrations of 125 μm to 1 mM had a pro-proliferative effect on bone mesenchymal stem cells, being 500 μm the optimal concentration [46]. This concentration, which equals to approximately 3.5 mg/L, was found, additionally, to activate Wnt signalling, needed for VEGF expression and bone regeneration, even in the presence of XAV-939 inhibitor [46]. In Fig. 4 it can be appreciated that for both scaffold and concentrations, lithium liberation remained above this value, being closer to 3.5 mg/L at 10 mg/L concentration. In addition, Clément-Lacroix et al. reported an increase in both bone mass and bone formation in mice treated with lithium chloride, a result of the activation of the Wnt canonical signalling [47]. Consequently, the liberation of lithium may contribute to the osteogenic and angiogenic potential of these scaffolds.

Regarding the constituting ions P and Si, an inverse relationship is evident between their respective concentrations: a reduction in phosphorus concentration is accompanied by an increase in silicon concentration, and *vice versa*. Given that the scaffolds are bioactive in SBF, and alpha-MEM is supersaturated with respect to HA, this could suggest the dissolution of a silicon-rich surface phase, followed by the precipitation of HA in a cyclic manner. This behaviour has already been described by Mata et al. [30]. Furthermore, this process is accompanied by a decline in magnesium levels, which may indicate the precipitation of Mg-enriched HA, as observed in bioactivity assays. While this would typically be expected to coincide with a decrease in calcium concentration, similar behaviour has been previously observed in our studies conducted in SBF [20,21]. This phenomenon may be attributed to a higher release of calcium from the scaffold, due to its high CaO content (37 wt%), which outpaces the rate of HA precipitation.

Lastly, the fluctuating behaviour of the doping ions sodium and potassium, which are consistently near baseline levels, may suggest that they could be incorporated as substituents in the precipitating and dissolving HA phases. This substitution is aligned with the dynamic ion exchange processes inherent to bioactive materials. The results suggest that, although there is no release of Mg^{2+}, Na^{+}, or K^{+}, in a context involving osteoclasts where the mineral phase is resorbed, these ions could still have a beneficial effect on osteogenic processes, particularly considering the crucial role of magnesium in osteogenic processes [28,48].

These mechanisms were accompanied by a change in pH. A general trend of alkalinisation was observed at concentrations of 100 mg/mL for both scaffolds. In contrast, at 10 mg/mL, the pH remained closer to control values, demonstrating a decrease by the end of the study. It has been previously demonstrated that an alkaline pH exerts beneficial effects on MC3T3-E1 preosteoblasts [49,50]. Gallow et al. reported that this alkalinisation not only enhanced the expression of genes typically activated at pH 7.4 but also induced the expression of additional genes related to osteogenesis [49]. Moreover, Gallow et al. observed enhanced MC3T3-E1 proliferation at pH levels between 8.2 and 8.8 [50].

In vitro biological characterisation of the scaffolds demonstrated their overall robust performance. WST-8 assays were conducted to evaluate the biocompatibility of the CM-IDP of the scaffolds and the material itself. The results demonstrated consistent cell population growth, confirming the biocompatibility of both the scaffold in solution and in solid form (Fig. 5). In the indirect approach, a lower cell viability was observed for CS04-100 mg/mL, particularly during the initial seven days of the study (Fig. 5A). From the ICP-OES results it can be concluded that this decrease is due to the increased release of silicon and combined with a pH of 9, which is above the level recommended by Gallow et al. [50]. Conversely, the findings from the direct approach (Fig. 5B) corroborate the biocompatibility of the scaffolds, as evidenced by the sustained proliferation of cells over time.

The biocompatibility of the material was further confirmed through fluorescence microscopy and SEM (Fig. 6). The cellular morphology observed during the indirect study revealed no differences between the treatment groups and the control, indicating that the IDP are cytocompatible (Fig. 6A). Additionally, in the direct approach, cells plated on the scaffolds displayed an extended morphology throughout the study, indicating a good cell-material interaction (Fig. 6B). If this were not the case, contracted cells minimising contact with the interface would have been observed.

Given the previous *in vitro* bioactivity (Fig. 3, Table 1) and ICP-OES results (Fig. 4) suggesting good osteogenic properties, the specific activity of alkaline phosphatase in cell lysates, a recognised marker of osteoblast differentiation, was quantified. The results showed a higher specific ALP activity compared to the control group. The high content of calcium phosphates in the scaffolds, mainly calcium pyrophosphate and β-TCP, together with its partially Mg-substituted phase, whitlockite, provides a substrate for the enzyme. This, together with the alkalinisation of the medium induced by SiO_4^{-4}, creates an optimal biochemical environment for ALP activity, as the enzyme functions more efficiently under alkaline conditions, which would explain its increased activity.

Calcium deposition was also evaluated using the ARS assay. The results showed the formation of mineralised nodules in the 2D control group after 14 days (Fig. 7A). Similarly, an increase in red staining was observed in both CS04 and CS05 scaffolds on day 14, with the effect becoming more pronounced after 21 days. These results are consistent with previous studies showing that the MC3T3-E1 subclone begins to deposit a well mineralised extracellular matrix (ECM) as early as 10 days [51]. In addition, Deliormanlı et al. reported comparable behaviour in MC3T3-E1 cells cultured on graphene-containing PCL/bioactive glass scaffolds, with a significant increase in mineralisation after 21 days [52].

These scaffolds also demonstrated their angiogenic potential, as evidenced by the stimulation of VEGF release compared to the control, which was detected from day 14 onwards. This, combined with their appropriate porosity could support the formation of a vascular network that infiltrates the scaffold, in turn facilitating tissue regeneration.

Conclusion

Third generation porous multilayer scaffolds were designed based on the SiO_2–CaO–P_2O_5 system, incorporating Li_2O, Na_2O, K_2O, and MgO (0.38; 0.49 wt%) as network modifiers. The MgO content was varied to optimise the physical, topographical, and biological properties of the scaffolds. While the physical characteristics remained unchanged, the MgO content influenced the scaffold's topography and bioactive behaviour, leading to the formation of either a lamellar structure (CS04) or the precipitation of HA hollow microspheres (CS05) upon 7-day SBF exposure.

In vitro biological characterisation yielded promising results in three key areas: (i) the scaffolds and their degradation products were biocompatible, promoting cellular proliferation and osteogenic processes, (ii) the scaffolds induced osteogenic differentiation, as evidenced by calcium deposit formation and increased ALP specific activity, and (iii) the scaffolds stimulated VEGF release by up to 170% compared to the control. The structural and functional optimisation potential of these scaffolds highlights their promise in addressing critical challenges in bone tissue engineering.

Future investigations will focus on studying the capacity for loading therapeutic agents, utilising the interlamellar spaces and hollow microspheres of the scaffolds. These structures offer significant potential for the localised delivery of bioactive molecules tailored to specific clinical needs. Moreover, preclinical studies in animal models will assess the osteoinductive and osteoconductive properties of the scaffolds, in addition to their effects on the quality of bone tissue, vascularisation, integration with the host bone, and immune response.

Acknowledgements

This work is part of the project PID2020-116693RB-C21, funded by MCIN/AEI/10.13039/501100011033 Spain.

REFERENCES

[1] B. Lunenfeld, P. Stratton, The clinical consequences of an ageing world and preventive strategies, Best Pract. Res. Clin. Obst. Gynaecol. 27 (5) (2013), http://dx.doi.org/10.1016/j.bpobgyn.2013.02.005.
[2] T. Mastnak, U. Maver, M. Finšgar, Addressing the needs of the rapidly aging society through the development of multifunctional bioactive coatings for orthopedic applications, Int. J. Mol. Sci. 23 (5) (2022), http://dx.doi.org/10.3390/ijms23052786.
[3] A.M. Wu, C. Bisignano, S.L. James, G.G. Abady, A. Abedi, E. Abu-Gharbieh, R.K. Alhassan, V. Alipour, J. Arabloo, M. Asaad, W.N. Asmare, A.F. Awedew, M. Banach, S.K. Banerjee, A. Bijani, T.T.M. Birhanu, S.R. Bolla, L.A. Cámera, J.C. Chang, T. Vos, Global, regional, and national burden of bone fractures in 204 countries and territories, 1990–2019: a systematic analysis from the Global Burden of Disease Study 2019, Lancet Healthy Longev. 2 (9) (2021), http://dx.doi.org/10.1016/S2666-7568(21)00172-0.
[4] E. Seeman, Pathogenesis of bone fragility in women and men, Lancet 359 (9320) (2002), http://dx.doi.org/10.1016/S0140-6736(02)08706-8.
[5] M.A. Clynes, N.C. Harvey, E.M. Curtis, N.R. Fuggle, E.M. Dennison, C. Cooper, The epidemiology of osteoporosis, Br. Med. Bull. 133 (1) (2020), http://dx.doi.org/10.1093/bmb/ldaa005.
[6] H. Newman, Y.V. Shih, S. Varghese, Resolution of inflammation in bone regeneration: from understandings to therapeutic applications, Biomaterials 277 (2021), http://dx.doi.org/10.1016/j.biomaterials.2021.121114.
[7] C.S. Bahney, R.L. Zondervan, P. Allison, A. Theologis, J.W. Ashley, J. Ahn, T. Miclau, R.S. Marcucio, K.D. Hankenson, Cellular biology of fracture healing, J. Orthop. Res. 37 (1) (2019), http://dx.doi.org/10.1002/jor.24170.
[8] L. Steppe, M. Megafu, M.E.A. Tschaffon-Müller, A. Ignatius, M. Haffner-Luntzer, Fracture healing research: recent insights, Bone Rep. 19 (2023), http://dx.doi.org/10.1016/j.bonr.2023.101686.
[9] X. Yu, X. Tang, S.V. Gohil, C.T. Laurencin, Biomaterials for bone regenerative engineering, Adv. Healthc. Mater. 4 (9) (2015) 1268–1285, http://dx.doi.org/10.1002/adhm.201400760.
[10] Ž. Perić Kačarević, P. Rider, S. Alkildani, S. Retnasingh, M. Pejakić, R. Schnettler, M. Gosau, R. Smeets, O. Jung, M. Barbeck, An introduction to bone tissue engineering, Int. J. Artif. Organs 43 (2) (2020), http://dx.doi.org/10.1177/0391398819876286.
[11] J. Henkel, M.A. Woodruff, D.R. Epari, R. Steck, V. Glatt, I.C. DIckinson, P.F.M. Choong, M.A. Schuetz, W. Di Hutmacher, Bone regeneration based on tissue engineering conceptions – a 21st century perspective, Bone Res. 1 (2013), http://dx.doi.org/10.4248/BR201303002.
[12] M. Navarro, A. Michiardi, O. Castaño, J.A. Planell, Biomaterials in orthopaedics, J. R. Soc. Interface 5 (27) (2008), http://dx.doi.org/10.1098/rsif.2008.0151.
[13] L.L. Hench, I. Thompson, Twenty-first century challenges for biomaterials, J. R. Soc. Interface 7 (SUPPL. 4) (2010), http://dx.doi.org/10.1098/rsif.2010.0151.focus.
[14] M. Vallet-Regí, A.J. Salinas, Ceramics as bone repair materials, in: bone repair biomaterials: regeneration and clinical applications, second edition, 2018, http://dx.doi.org/10.1016/B978-0-08-102451-5.00006-8.
[15] H. Ismail, H. Mohamad, Bioactivity and biocompatibility properties of sustainable wollastonite bioceramics from rice husk ash/rice straw ash: a review, Materials 14 (18) (2021), http://dx.doi.org/10.3390/ma14185193.

[16] A.R. Amini, C.T. Laurencin, S.P. Nukavarapu, Bone tissue engineering: recent advances and challenges, Crit. Rev. Biomed. Eng. 40 (5) (2012), http://dx.doi.org/10.1615/CritRevBiomedEng.v40.i5.10.
[17] Á.E. Mercado-Pagán, A.M. Stahl, Y. Shanjani, Y. Yang, Vascularization in bone tissue engineering constructs, Ann. Biomed. Eng. 43 (3) (2015), http://dx.doi.org/10.1007/s10439-015-1253-3.
[18] H.-H. Lu, D. Ege, S. Salehi, A.R. Boccaccini, Ionic medicine: exploiting metallic ions to stimulate skeletal muscle tissue regeneration, Acta Biomater. 190 (2024) 1–23, http://dx.doi.org/10.1016/j.actbio.2024.10.033.
[19] F.E. Ciraldo, E. Boccardi, V. Melli, F. Westhauser, A.R. Boccaccini, Tackling bioactive glass excessive in vitro bioreactivity: preconditioning approaches for cell culture tests, Acta Biomater. 75 (2018), http://dx.doi.org/10.1016/j.actbio.2018.05.019.
[20] P.M. Riosalido, P. Velásquez, Á. Murciano, P.N. De Aza, Surface morphology modulation in multilayer scaffolds via ion doping for bone tissue engineering, J. Am. Ceram. Soc. Am. Ceram. Soc. 108 (3) (2025), http://dx.doi.org/10.1111/jace.20269.
[21] P.M. Riosalido, P. Velásquez, Á. Murciano, P.N. De Aza, Multilayer scaffolds designed with bioinspired topography for bone regeneration, Ceram. Int. (2025), http://dx.doi.org/10.1016/j.ceramint.2025.01.180.
[22] International Organisation for Standardisation. Implants for surgery—*in vitro* evaluation for apatite-forming ability of implant materials (ISO Standard No. 23317:2014) (2014).
[23] Mouse VEGF ELISA Kit. (2024). RayBiotech. https://doc.raybiotech.com/pdf/Manual/ELM-VEGF.pdf.
[24] Q. Liu, S. Huang, J.P. Matinlinna, Z. Chen, H. Pan, Insight into biological apatite: physiochemical properties and preparation approaches, BioMed Res. Int. 2013 (2013), http://dx.doi.org/10.1155/2013/929748.
[25] C. Combes, S. Cazalbou, C. Rey, Apatite biominerals, Minerals 6 (2) (2016), http://dx.doi.org/10.3390/min6020034.
[26] D. Stachel, H. Paulus, I. Svoboda, H. Fuess, Crystal structure of calcium ultraphosphate, $Ca_2P_6O_{17}$, Zeitschrift Fur Kristallographie – New Cryst. Struct. 202 (1–2) (1992), http://dx.doi.org/10.1524/zkri.1992.202.1-2.117.
[27] K.H. Min, D.H. Kim, K.H. Kim, J.-H. Seo, S.P. Pack, Biomimetic scaffolds of calcium-based materials for bone regeneration, Biomimetics 9 (9) (2024) 511, http://dx.doi.org/10.3390/biomimetics9090511.
[28] A. Hoppe, N.S. Güldal, A.R. Boccaccini, A review of the biological response to ionic dissolution products from bioactive glasses and glass-ceramics, Biomaterials 32 (11) (2011), http://dx.doi.org/10.1016/j.biomaterials.2011.01.004.
[29] M. Sanmartin de Almeida, G.V. de O. Fernandes, A.M. de Oliveira, J.M. Granjeiro, Calcium silicate as a graft material for bone fractures: a systematic review, J. Int. Med. Res. 46 (7) (2018), http://dx.doi.org/10.1177/0300060518770940.
[30] N.A. Mata, P. Velasquez, A. Murciano, P.N. de Aza, Multilayer Mg-pyrophosphate glass ceramic with discontinuous bioactivity. Physicochemical characterization, Ceram. Int. 47 (10) (2021), http://dx.doi.org/10.1016/j.ceramint.2021.02.044.
[31] D. Griesiute, A. Kizalaite, A. Dubnika, V. Klimavicius, V. Kalendra, V. Tyrpekl, S.H. Cho, T. Goto, T. Sekino, A. Zarkov, A copper-containing analog of the biomineral whitlockite: dissolution–precipitation synthesis, structural and biological properties, Dalton Trans. 53 (4) (2023), http://dx.doi.org/10.1039/d3dt03756h.
[32] L. Bauer, M. Antunović, A. Rogina, M. Ivanković, H. Ivanković, Bone-mimetic porous hydroxyapatite/whitlockite scaffolds: preparation, characterization and interactions with human mesenchymal stem cells, J. Mater. Sci. 56 (5) (2021), http://dx.doi.org/10.1007/s10853-020-05489-3.
[33] A.M. Weatherholt, R.K. Fuchs, S.J. Warden, Specialized connective tissue: bone, the structural framework of the upper extremity, J. Hand Therapy 25 (2) (2012), http://dx.doi.org/10.1016/j.jht.2011.08.003.
[34] G. Kaur, V. Kumar, F. Baino, J.C. Mauro, G. Pickrell, I. Evans, O. Bretcanu, Mechanical properties of bioactive glasses, ceramics, glass-ceramics and composites: state-of-the-art review and future challenges, Mater. Sci. Eng. C 104 (2019), http://dx.doi.org/10.1016/j.msec.2019.109895.
[35] N. Tamai, A. Myoui, T. Tomita, T. Nakase, J. Tanaka, T. Ochi, H. Yoshikawa, Novel hydroxyapatite ceramics with an interconnective porous structure exhibit superior osteoconduction in vivo, J. Biomed. Mater. Res. 59 (1) (2002), http://dx.doi.org/10.1002/jbm.1222.
[36] N. Abbasi, A. Abdal-Hay, S. Hamlet, E. Graham, S. Ivanovski, Effects of gradient and offset architectures on the mechanical and biological properties of 3-D Melt Electrowritten (MEW) scaffolds, ACS Biomater. Sci. Eng. 5 (7) (2019), http://dx.doi.org/10.1021/acsbiomaterials.8b01456.
[37] H.L. Jang, G. bin Zheng, J. Park, H.D. Kim, H.R. Baek, H.K. Lee, K. Lee, H.N. Han, C.K. Lee, N.S. Hwang, J.H. Lee, K.T. Nam, In vitro and in vivo evaluation of whitlockite biocompatibility: comparative study with hydroxyapatite and β-tricalcium phosphate, Adv. Healthc. Mater. 5 (1) (2016), http://dx.doi.org/10.1002/adhm.201400824.
[38] F. Ren, Y. Leng, R. Xin, X. Ge, Synthesis, characterization and ab initio simulation of magnesium-substituted hydroxyapatite, Acta Biomater. 6 (7) (2010), http://dx.doi.org/10.1016/j.actbio.2009.12.044.
[39] T. Sugimoto, M. Kanatani, J. Kano, H. Kaji, T. Tsukamoto, T. Yamaguchi, M. Fukase, K. Chihara, Effects of high calcium concentration on the functions and interactions of osteoblastic cells and monocytes and on the formation of osteoclast-like cells, J. Bone Miner. Res. 8 (12) (1993), http://dx.doi.org/10.1002/jbmr.5650081206.
[40] S. Jiang, M. Wang, J. He, A review of biomimetic scaffolds for bone regeneration: toward a cell-free strategy, Bioeng. Transl. Med. 6 (2) (2021), http://dx.doi.org/10.1002/btm2.10206.
[41] K.M. Son, H.C. Park, N.R. Kim, I.S. Lee, H.C. Yang, Enhancement of the ALP activity of C3H10T1/2 cells by the combination of an oxysterol and apatite, Biomed. Mater. 5 (4) (2010), http://dx.doi.org/10.1088/1748-6041/5/4/044107.
[42] W. Götz, E. Tobiasch, S. Witzleben, M. Schulze, Effects of silicon compounds on biomineralization, osteogenesis, and hard tissue formation, Pharmaceutics 11 (3) (2019), http://dx.doi.org/10.3390/pharmaceutics11030117.
[43] K. Jiao, L.N. Niu, Q.H. Li, F.M. Chen, W. Zhao, J.J. Li, J.H. Chen, C.W. Cutler, D.H. Pashley, F.R. Tay, Biphasic silica/apatite co-mineralized collagen scaffolds stimulate osteogenesis and inhibit RANKL-mediated osteoclastogenesis, Acta Biomater. 19 (2015), http://dx.doi.org/10.1016/j.actbio.2015.03.012.
[44] J. Sun, J. Li, X. Liu, L. Wei, G. Wang, F. Meng, Proliferation and gene expression of osteoblasts cultured in DMEM containing the ionic products of dicalcium silicate coating, Biomed. Pharmacother. 63 (9) (2009), http://dx.doi.org/10.1016/j.biopha.2009.01.007.
[45] L. Liu, Y. Liu, C. Feng, J. Chang, R. Fu, T. Wu, F. Yu, X. Wang, L. Xia, C. Wu, B. Fang, Lithium-containing biomaterials stimulate bone marrow stromal cell-derived exosomal miR-130a secretion to promote angiogenesis, Biomaterials 192 (2019), http://dx.doi.org/10.1016/j.biomaterials.2018.11.007.
[46] Z. Tan, B. Zhou, J. Zheng, Y. Huang, H. Zeng, L. Xue, D. Wang, Lithium and copper induce the osteogenesis-angiogenesis coupling of bone marrow mesenchymal stem cells via crosstalk between canonical Wnt and HIF-1 α signaling

pathways, Stem Cells Int. 2021 (2021), http://dx.doi.org/10.1155/2021/6662164.
[47] P. Clément-Lacroix, M. Ai, F. Morvan, S. Roman-Roman, B. Vayssière, C. Belleville, K. Estrera, M.L. Warman, R. Baron, G. Rawadi, Lrp5-independent activation of Wnt signaling by lithium chloride increases bone formation and bone mass in mice, Proc. Natl. Acad. Sci. U.S.A. 102 (48) (2005), http://dx.doi.org/10.1073/pnas.0505259102.
[48] E. O'Neill, G. Awale, L. Daneshmandi, O. Umerah, K.W.H. Lo, The roles of ions on bone regeneration, Drug Discov. Today 23 (4) (2018), http://dx.doi.org/10.1016/j.drudis.2018.01.049.
[49] A.M. Galow, A. Rebl, D. Koczan, J. Gimsa, MC3T3 osteoblast-like cells cultured at alkaline pH: microarray data (Affymetrix GeneChip Mouse 2.0 ST), Data Brief 13 (2017), http://dx.doi.org/10.1016/j.dib.2017.05.013.
[50] A.M. Galow, A. Rebl, D. Koczan, S.M. Bonk, W. Baumann, J. Gimsa, Increased osteoblast viability at alkaline pH in vitro provides a new perspective on bone regeneration, Biochem. Biophys. Rep. 10 (2017), http://dx.doi.org/10.1016/j.bbrep.2017.02.001.
[51] D. Wang, K. Christensen, K. Chawla, G. Xiao, P.H. Krebsbach, R.T. Franceschi, Isolation and characterization of MC3T3-E1 preosteoblast subclones with distinct in vitro and in vivo differentiation/mineralization potential, J. Bone Miner. Res. 14 (6) (1999), http://dx.doi.org/10.1359/jbmr.1999.14.6.893.
[52] A.M. Deliormanlı, H. Atmaca, Biological response of osteoblastic and chondrogenic cells to graphene-containing PCL/bioactive glass bilayered scaffolds for osteochondral tissue engineering applications, Appl. Biochem. Biotechnol. 186 (4) (2018), http://dx.doi.org/10.1007/s12010-018-2758-7.